Supplementary Information for: Long-range temporal coordination of gene expression in synthetic microbial consortia

Jae Kyoung Kim[1,*,‡], Ye Chen[2,*,†], Andrew J. Hirning[2], Razan N. Alnahhas[2], Krešimir Josić[2,3,4,‡], and Matthew R. Bennett[2,5,6,‡]

1. Department of Mathematics, Korean Advanced Institute of Science and Technology, Daejeon, South Korea.

2. Department of Biosciences, Rice University, Houston, TX.

3. Department of Mathematics, University of Houston, Houston, TX.

4. Department of Biology and Biochemistry, University of Houston, Houston, TX.

5. Department of Bioengineering, Rice University, Houston, TX.

6. Lead contact.

* Equal contribution.

† Current address: Department of Bioengineering, Massachusetts Institute of Technology, Boston, MA.

‡ Correspondence: matthew.bennett@rice.edu, josic@math.uh.edu, jaekkim@kaist.ac.kr.

Supplementary Table 1 List of model variables and their descriptions.

Name	Description
R_a	The concentration of RhlI in the intracellular space of the activator strain
C_r	The concentration of CinI in the intracellular space of the repressor strain
$L_{a/r}$	The concentration of LacI in the intracellular space of the activator/repressor strain
$A_{a/r}$	The concentration of AiiA in the intracellular space of the activator/repressor strain
F_a	The concentration of premature CFP in the intracellular space of the activator strain
M_a	The concentration of mature CFP in the intracellular space of the activator strain
Y_r	The concentration of premature YFP in the intracellular space of the repressor strain
M_r	The concentration of mature YFP in the intracellular space of the repressor strain
$H_{a/r/e}$	The concentration of C4-HSL in the activator strain/repressor strain/extracellular space.
$I_{a/r/e}$	The concentration of 3-OHC14-HSL in the activator strain/repressor strain/extracellular space.

Supplementary Table 2 List of model parameters and the values used for simulations. References are shown for values obtained from the literature.

Name	Description	Value	Reference
η_{R0}	Basal production rate of RhlI via $P_{rhl/lac-s}/P_{lac}$	$20.13/177.44*\mathbf{S_R}$ nM min^{-1}	Chen et al., 2015
η_{R1}	Maximal production rate of RhlI with C4 via $P_{rhl/lac-s}/P_{lac}$	$367.48/0*\mathbf{S_R}$ nM min^{-1}	Chen et al., 2015
η_{C0}	Basal production rate of CinI via $P_{rhl/lac-w}$	$1*\mathbf{S_C}$ nM min^{-1}	Chen et al., 2015
η_{C1}	Maximal production rate of CinI with C4 via $P_{rhl/lac-w}$	$624.44*\mathbf{S_C}$ nM min^{-1}	Chen et al., 2015
η_{F0}	Basal production rate of CFP via $P_{rhl/lac-s}/P_{lac}$	$20.13/177.44*\mathbf{S_F}$ nM min^{-1}	Chen et al., 2015
η_{F1}	Maximal production rate of CFP with C4 via $P_{rhl/lac-s}/P_{lac}$	$367.48/0*\mathbf{S_F}$ nM min^{-1}	Chen et al., 2015
η_{Y0}	Basal production rate of YFP via $P_{cin/lac-m}$	$41.8*\mathbf{S_Y}$ nM min^{-1}	Chen et al., 2015
η_{Y1}	Maximal production rate of YFP with C14 via $P_{cin/lac-m}$	$197.49*\mathbf{S_Y}$ nM min^{-1}	Chen et al., 2015
η_{L0}	Basal production rate of LacI via P_{cin}	$1*\mathbf{S_L}$ nM min^{-1}	Chen et al., 2015
η_{L1}	Maximal production rate of LacI with C14 via P_{cin}	$1735.47*\mathbf{S_L}$ nM min^{-1}	Chen et al., 2015
η_{A0}	Basal production rate of AiiA via P_{cin*}	$27.03*\mathbf{S_A}$ nM min^{-1}	Chen et al., 2015
η_{A1}	Maximal production rate of AiiA with C14 via P_{cin*}	$141.61*\mathbf{S_A}$ nM min^{-1}	Chen et al., 2015
K_H	EC50 of C4 for $P_{rhl/lac-w}/P_{rhl/lac-s}$	$16599/5937$ nM	Lamb et al., 2003; Chen et al., 2015
K_L	IC50 of LacI for $P_{rhl/lac}$ ($P_{cin/lac}$)/P_{lac} in the presence of 1mM IPTG	$47.7/85.38$ nM	Block et al., 2012; Chen et al., 2015
K_I	EC50 of C14 for P_{cin} ($P_{cin/lac-w}$)/P_{cin*} ($P_{cin/lac-m}$)	$2357.3/594.23$ nM	Chen et al., 2015
n_H	Hill coefficient of C4 for $P_{rhl/lac-w}$ and $P_{rhl/lac-s}$	4	Chen et al., 2015
n_L	Hill coefficient of LacI for $P_{rhl/lac-w}$ and $P_{rhl/lac-s}$	2	Chen et al., 2015
n_I	Hill coefficient of C14 for P_{cin}, P_{cin*}, $P_{cin/lac-w}$, $P_{cin/lac-m}$	4	Chen et al., 2015
d_c	Catalytic constant of ClpXP for $ssrA$-tagged protein degradation (RhlI/CinI/AiiA/LacI/CFP/YFP)	$1.8*\mathbf{S_{ClpXP}}$ nM min^{-1}	Burton et al., 2001; Farrell et al., 2007; Flynn et al., 2001
K_c	Half-maximal constant of ClpXP for $ssrA$-tagged protein degradation (RhlI/CinI/AiiA/LacI/CFP/YFP)	1300 nM	Burton et al., 2001; Farrell et al., 2007; Flynn et al., 2001
d_A	Catalytic constant of AiiA for C4 and C14 degradation	2257 min^{-1}	Wang et al., 2004; Thomas et al., 2005
K_A	Half-maximal constant of AiiA for C4 and C14 degradation	5110 μM	Wang et al., 2004; Thomas et al., 2005
d	Intracellular dilution rate due to cell growth	ln(2)/25 min^{-1}	Volfson et al., 2008
μ_e	Extracellular dilution rate due to media flow	0.1 min^{-1}	Prindle et al., 2014
π_H	Export rate of C4	3 min^{-1}	Pai and You, 2009
π_I	Export rate of C14	2.1 min^{-1}	Pai and You, 2009
ϕ_H	Production rate of C4 by RhlI	16 min^{-1}	Pai and You, 2009; Parsek et al., 1999
ϕ_I	Maximal production rate of C14 by CinI	2 min^{-1}	Pai and You, 2009; Schaefer et al., 1996
m	Maturation rate of CFP and YFP	ln(2)/3 min^{-1}	Nagai et al., 2002
d_e	Volume fraction of extracellular space in chamber	0.2	Volfson et al., 2008
τ	Time delay for transcription and translation	7.5 min	Gedeon and Bokes, 2012
D_H	Diffusion coefficient of C4	4800 μm^2 min^{-1}	Danino et al., 2010
D_I	Diffusion coefficient of C14	3360 μm^2 min^{-1}	Pai and You, 2009

Values for the indeterminant parameter values (shown in **bold**) are S_R=3.06, S_C=37.23, S_L=4.52, S_A=9.54, S_F=113, S_Y=6.8, and S_{ClpXP}=1820.

Supplementary Table 3 List of plasmids used in this study.

| Plasmid	Open reading frame(s)	Origin/Resistance
pC165	P_{lac}-rhlI; P_{lac}-cfp	pMB1+rop, Kan^R
pC247	$P_{rhl/lac-s}$-rhlI; $P_{rhl/lac-s}$-cfp	pMB1+rop, Kan^R
pC365	$P_{rhl/lac-w}$-cinI; $P_{cin/lac-s}$-yfp	pMB1+rop, Kan^R
pC235	P_{cin}←-aiiA	p15A, Spec^R
pC239	P_{cin}-lacI; P_{cin}←-aiiA	p15A, Spec^R
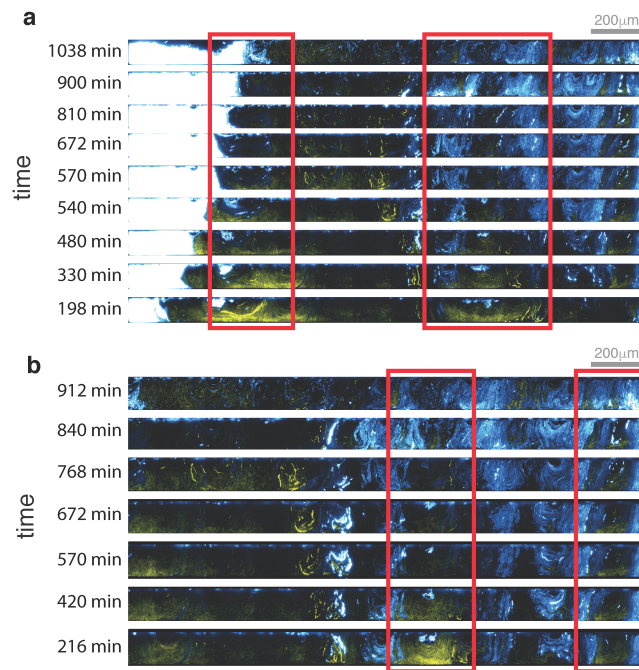
Supplementary Figure 1 Representative fluorescence images of cells growing in the extended hallway device (Fig. 1b). (a, b) A chamber with a wall leads to unstable spatial arrangement of the two strains, which we highlighted using red boxes (n=3 independent experiments).
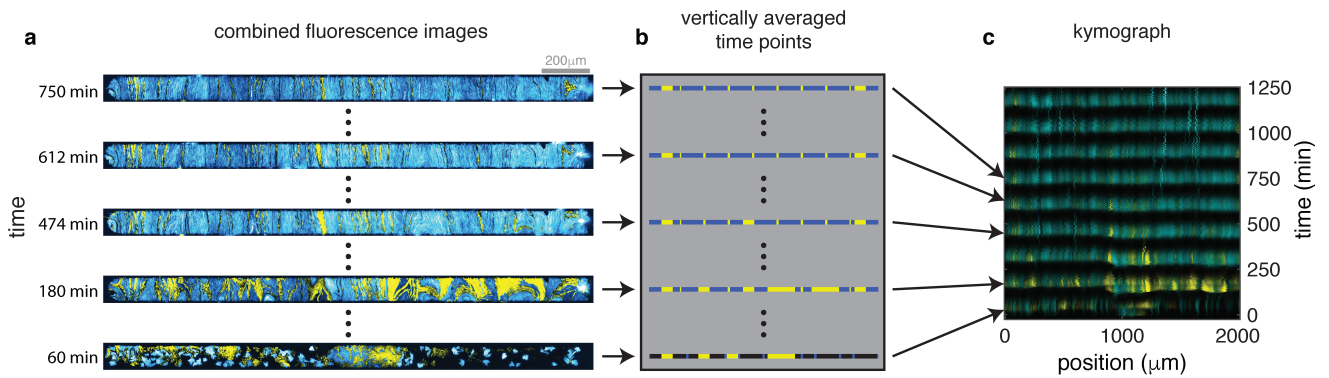
Supplementary Figure 2 Illustration for the process of generating kymograph from fluorescence images. (a-c) The fluorescence images at each time (a) are vertically averaged (b) as the height of the chamber is much shorter than the width (Fig. 1b and d). The vertically averaged values are merged along the time to construct the kymograph (c): each pixel in this plot represents the average color across a vertical line of pixels in the chamber at a given time. Thus, the kymograph describes the dynamical changes in the level fluorescence of the two channels (colors) as a function of time (vertical axis) and horizontal position in the chamber (horizontal axis).
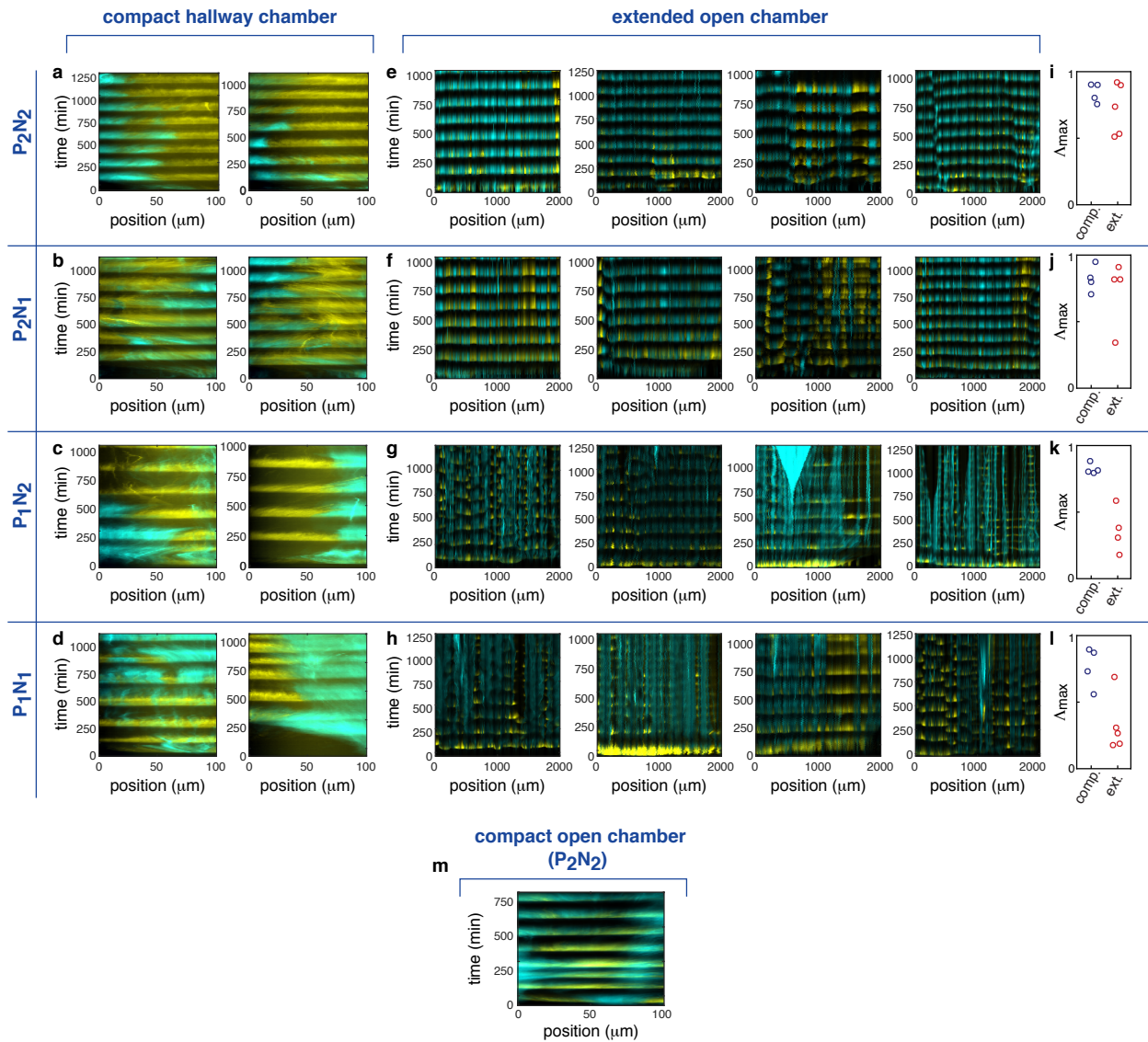
Supplementary Figure 3 Comparison of the two-strain oscillators with different network architectures in the compact hallway (a-d), extended open (e-h) and compact open chamber (m) (n=4 independent experiments for each of these except (e) and (h) for which n=5 and (m) for which n=1). (a-l) The synchrony of the oscillations across the chamber is quantified using the largest eigenvalue of the equal-time correlation matrix normalized by the dimension of the matrix (Λ_{max}) (i-l). Here, Λ_{max} equals 1 when oscillations across the entire chamber are synchronous (See Methods for details). Unlike the compact chamber, the positive feedback loop is required to generate synchronized oscillations in the extended chamber. The mean of Λ_{max} is not different between the architectures with and without positive feedback in the compact chamber (p=0.46, two-sided Welch's t-test, n=8 independent experiments). However, in the extended chamber the difference of means is significant (p=8.8x10^{-4}, two-sided Welch's t-test, n=9 independent experiments). Here, the kymographs in the compact *hallway* chamber are obtained by reanalyzing our previous published data[3]. (m) The kymograph of a P$_2$N$_2$ consortium in the compact open chamber shows synchronous oscillations across the chamber consistent with those observed in the compact hallway chambers (a). Due to the small size of the chamber, and the effects of the wedge at the right end of the trap, the spatial distribution and ratio of the two strains fluctuate over time, as in the case of the hallway chamber (a), but different from the extended open chambers (e). The design of the chamber (i.e. open and hallway) does not seem to have a strong effect on the spatio-temporal dynamics of the consortium when the size of the chamber is small.
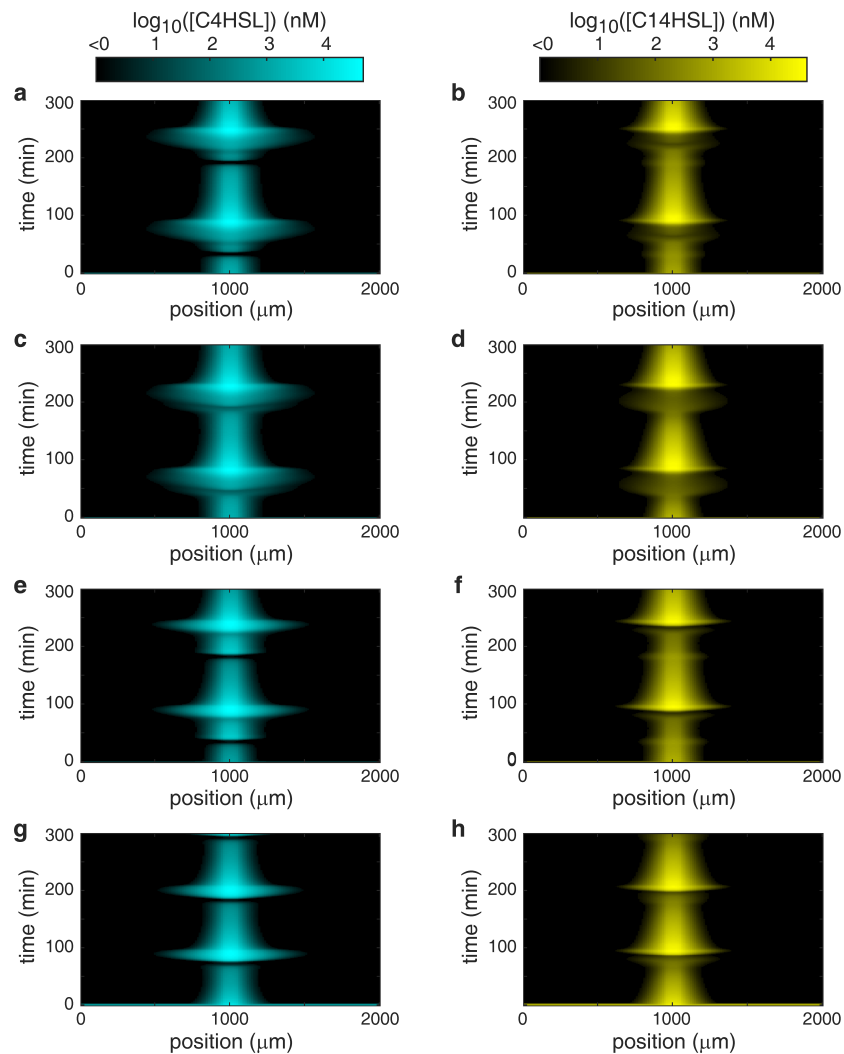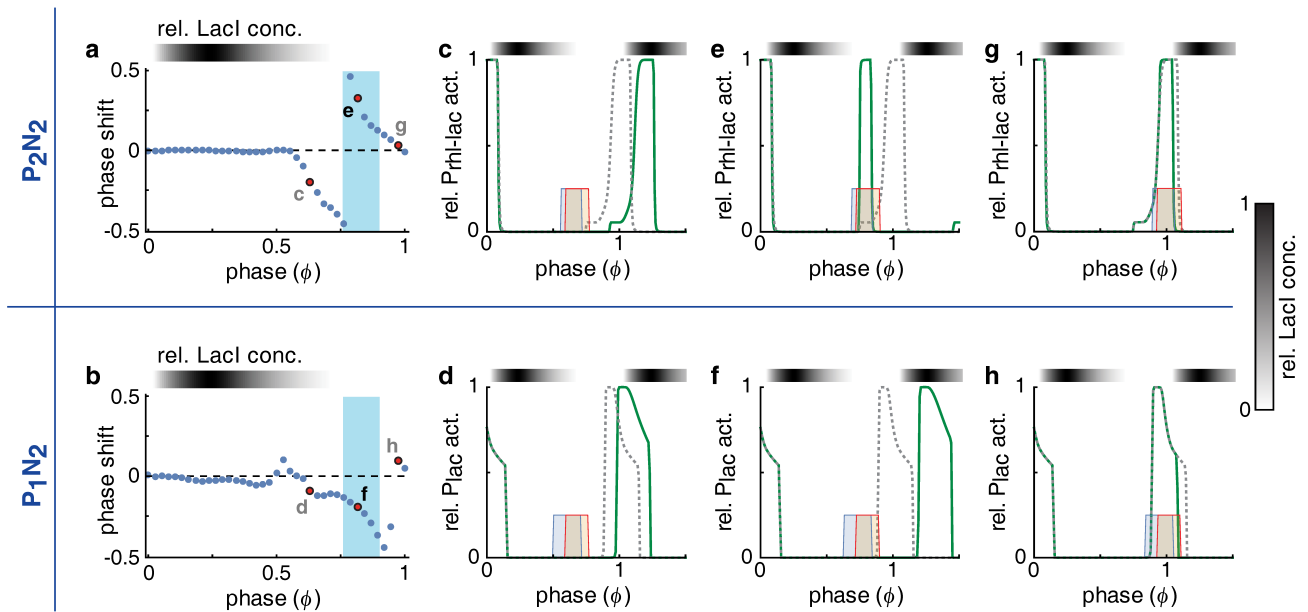
Supplementary Figure 4 The range of signaling molecules in the model with different architectures. (a,c,e,g) C4HSL generated by a population that extends 100µm across the middle of the chamber is tracked for the model with the architecture of P_2N_2 (a), P_2N_1 (c), P_1N_2 (e) and P_1N_1 (g). (b,d,f,h) Same as (a,c,e,g), but for the C14HSL (n=1 independent simulations for each). Both the activator signaling molecule (C4HSL) and repressor signaling molecule (C14HSL) diffuse a similar distance from a localized source in each of the four network architectures. Therefore, the four different architectures do not differ in the degree of coupling between neighboring populations. Furthermore, the relatively short range of diffusion from a localized source indicates that the synchronous behavior observed in Fig. 3 is not due to strong coupling between distant subpopulations in our model.
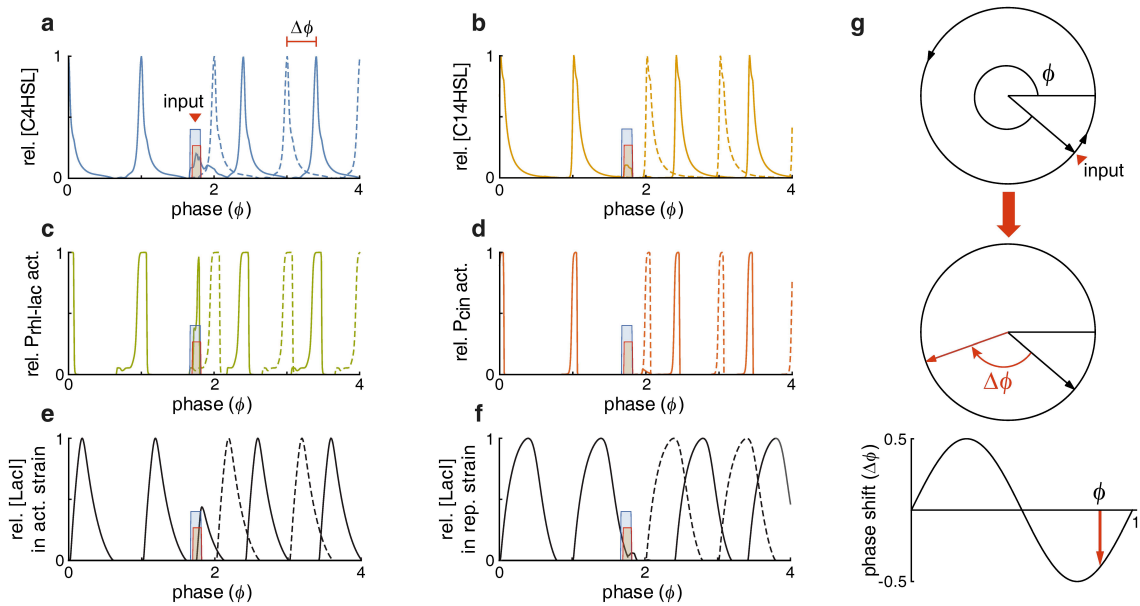
Supplementary Figure 5 Estimation of the phase shift in one subpopulation due to a signal from a neighboring subpopulation. (a-f) A phase shift ($\Delta\phi$) in the oscillation of a receiving population due to a pulsatile signal from a source population (Figs. 4a-b) was estimated by computing the phase difference between trajectories in the presence (solid line) and absence of the pulse (dashed line). To simulate the signal from the distant population we increased the diffusion rate of C4HSL and C14HSL in the simulation with a temporal profile that approximated the increase at $\Delta x = 50 \mu m$ from a source population (colored boxes). Note that the phases of key molecular concentrations and promoter activities are shifted together. Thus, the phase of a single molecule, C4HSL, is enough to estimate the phase shift in the model (Fig. 4c). (g) A schematic representation of the phase response curve (PRC): The advance or delay in the phase is computed as a function of the phase at which the pulsatile driving signal is received.
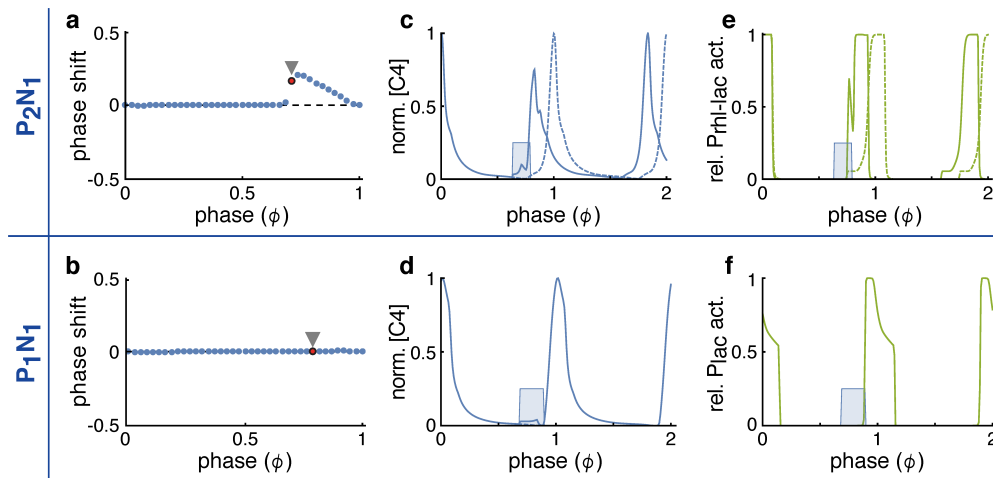
Supplementary Figure 6 The phase shift in simulated P_2N_1 and P_1N_1 architectures resulting from a pulsatile extracellular *activator* signal. (a-b) The extracellular activator signal pulse has little effect on the phase in the P_1N_1 architecture (b). However, the same pulse advances the phase of an oscillating subpopulation with P_2N_1 architecture when the promoter is not suppressed (e.g. the red circle in (a)). (c-f) When an extracellular activator signal pulse is received at the appropriate phase (e.g. the red circle in (a)) (c), the intracellular positive feedback loop in a P_2N_1 subpopulation is triggered (e). This leads to a local amplification of activator signal production (c) and the advance of the oscillation phase of the receiving population (e). In contrast, in the absence of a positive feedback loop in P_1N_1, such amplification does not occur, and hence there is no observable phase shift (d, f). Here, solid and dashed lines indicate the trajectories in the presence and absence of the extracellular signal, respectively.

Supplementary Figure 7 A pulsatile increase in both activator and repressor signaling molecule diffusion rate leads to a larger phase advance for the P_2N_2 architecture over the P_1N_2 architecture. (a-b) Phase response curves of P_2N_2 (a) and P_1N_2 (b) in response to the both activator and repressor signals. The simulations are as described in Fig. 4a and b. (c-h) When the concentration of LacI is decreasing (at $\phi \sim 0.5$ in Fig. 5e, f), a received repressor signal delays the de-repression of the repressed promoter, and thus delays the resulting phase in both P_2N_2 (c) and P_1N_2 (d). When the LacI is depleted and both promoters begin to turn on (at $\phi \sim 0.75$ in Supplementary Fig. 5c-f), P_2N_2 and P_1N_2 architectures exhibit *different* responses: The driving activator signal advances the activation of the promoter in the P_2N_2 (e), but not in the P_1N_2 architecture (f). In the absence of the positive feedback, the activator signal by itself is not sufficient to activate the promoters (*e.g.* P_{lac}) (Supplementary Fig. 6b, d, f). Instead, the repressor signal prevents the activation of the promoters and thus delays the phase. In contrast, in the presence of the positive feedback, the effect of the driving activator signal is amplified via the positive feedback loop (Supplementary Fig. 6a, c, e), which accelerates the activation of the promoter (*e.g.* $P_{rhl/lac}$) and advances the phase of the oscillator. Finally, if the pulse arrives when the promoter is fully activated ($\phi \sim 0.9$) (Supplementary Fig. 5c-f), the driving repressor signal accelerates the deactivation of the promoter and advances the phase in both P_2N_2 (g) and P_1N_2 (h) architectures.
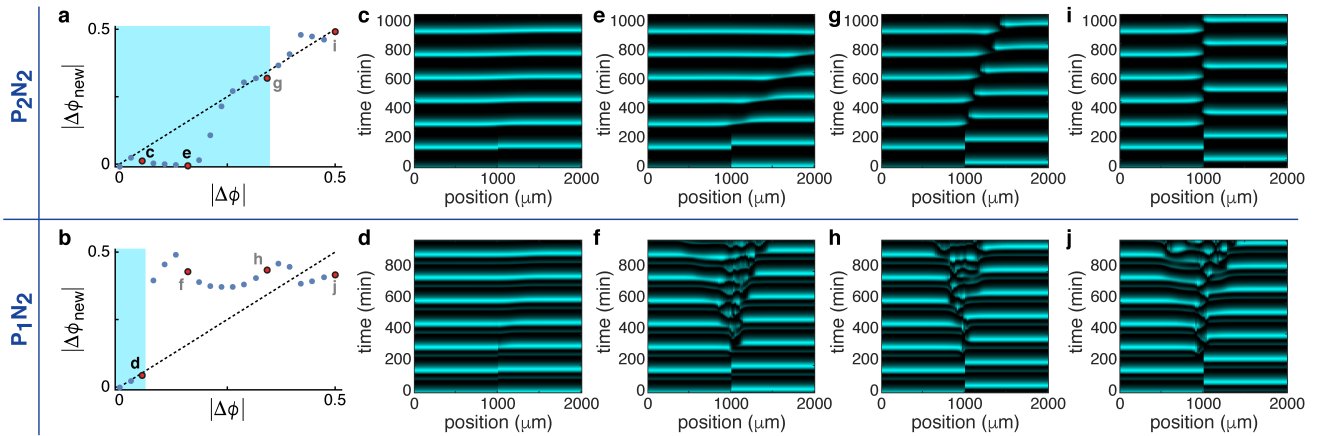
Supplementary Figure 8 Intracellular positive feedback loops promote synchronization. (a, b) The map of the phase difference, $\Delta\varphi_{new}$, after one oscillation cycle as a function of the initial phase difference, $\Delta\varphi$ (see Online Methods for details). Two coupled subpopulations with P_2N_2 architecture (a) display a wider range of initial phase differences, $\Delta\varphi$, which decrease after one cycle (i.e. $|\Delta\varphi_{new}|<|\Delta\varphi|$) compared to subpopulations with P_1N_2 architecture (b) (this region is shaded in blue). This predicts that a larger set of initial phase differences would lead to synchronization for the P_2N_2 architecture compared to the P_1N_2 architecture. (c-j) Two extended subpopulations with a range of initial phase differences (red circles in (a, b)) lead to different spatio-temporal dynamics for the two architecture types (n=1 independent simulation for each). When two coupled subpopulations start with a phase difference, $\Delta\varphi$=0.1, they are nearly synchronized after one oscillatory cycle in both architectures, P_2N_2 (c) and P_1N_2 (d). However, when the initial phase difference is $\Delta\varphi$=0.3, which is inside of the blue zone for the P_2N_2 architecture, but not the P_1N_2 architecture, the two subpopulations synchronize for the P_2N_2 (e), but not the P_1N_2 (f) architecture. Initial phase differences at the boundary of the blue zone for P_2N_2 and outside of the zone for P_1N_2, lead to synchrony for P_2N_2 but after a larger number of cycles compared to the previous cases (g), and no synchrony for P_1N_2 (h). When the initial phase difference is outside of the blue zones of both architectures, the two subpopulations eventually oscillate in anti-phase in both cases (i, j). These results suggest the biochemical mechanisms that drive synchronization. When the promoter of the trailing subpopulation is activated and subsequently releases a signal (*i.e.* HSL), the promoter of the leading subpopulation is already suppressed. The signal from the delayed subpopulation therefore has little effect on the phase of the leading subpopulation. In contrast, when the leading subpopulation releases its signal, the promoter of the trailing subpopulation may not be suppressed, and its phase can be shifted. In the presence of a positive feedback loop, when the leading subpopulation releases a signal before the trailing subpopulation promoter is activated, the activator signal accelerates the activation of the promoter of the trailing subpopulation. This *advances* its phase, and decreases the phase difference between the subpopulations (c, e, g). In the absence of a positive feedback loop, the repressor signal dominates and *delays* the activation of the promoter of the trailing subpopulation (the wide phase delay zone in Supplementary Fig. 7b). This increases the phase difference between the subpopulations (f, h, j). We can extend these ideas to multiple interacting subpopulations with each subpopulation receiving signals from both leading and trailing subpopulations. As described above, the signals from trailing subpopulations have little effect on the phase of a leading subpopulation. However, in the presence of a positive feedback loop, the effect of the activator signal from a leading subpopulation is amplified and the phase is advanced. This reduces the phase difference between the leading and recipient subpopulations, as long as their initial phase difference was not too large (*e.g.* the blue zone in Supplementary Fig. 8a). Subpopulations starting close to anti-phase will have little influence on each other, as signals reach the other subpopulation when the promoter is fully suppressed. In summary, a positive feedback loop can reduce phase differences among multiple subpopulations and lead to global synchrony provided initial phase differences are not too large.
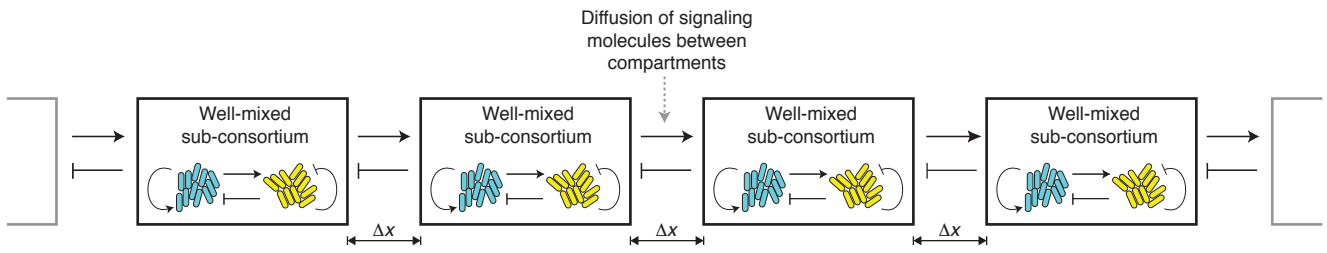
Supplementary Figure 9 A schematic of the spatial discretization used in our numerical model. To simulate the spatio-temporal dynamics of the consortium (Fig. 3), the chamber was divided into 100 compartments of equal size, $\Delta x=20\mu m$ (see Methods for details). Signaling molecules that were expressed within a compartment could diffuse only to neighboring compartments.
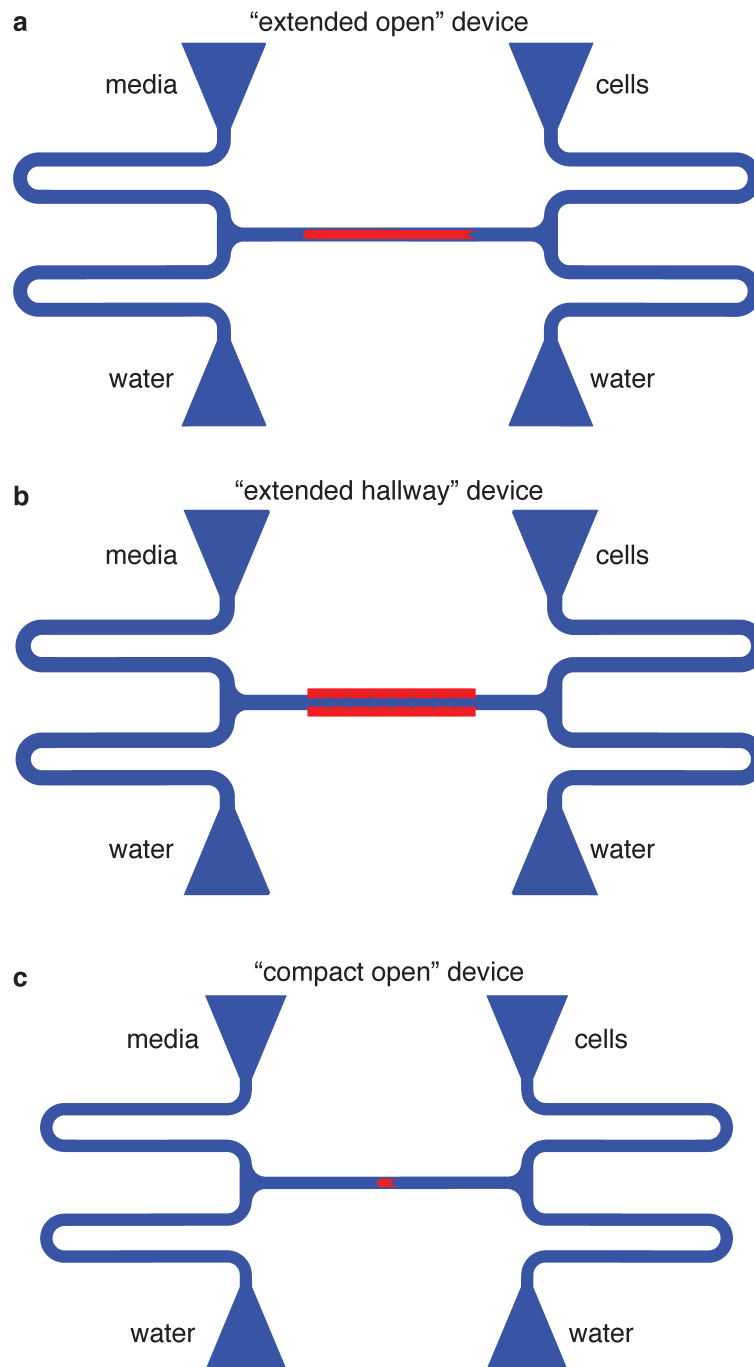
Supplementary Figure 10. Schematics of each of the microfluidic devices used in this study. (a) The "extended open" device. The trapping chamber (shown in red) is 2000 μm long, 100 μm wide, and 0.95 μm tall. (b) The "extended hallway" device. The trapping chamber (shown in red) is 2000 μm wide, 85 μm deep, and 1.6 μm tall. (c) The "compact open" device. The trapping chamber (shown in red) is 230 μm long, 100 μm wide, and 0.95μm tall. In each schematic, the flow channels (shown in blue) are 10 μm tall. The dynamics of growth and cell-cell signaling depends strongly on trap geometry[17]: In compact traps, diffusion is fast, and cells easily signal one another. However, the proportions of different strains within the trap can undergo large fluctuations. On the other hand, in the extended open traps, the relative ratio of strains is stable, but intercellular signaling is hindered by distances between cells. Different strategies, including how the population is seeded, can be used to navigate these tradeoffs[17].

Supplementary Video 1 Synchronous oscillations within a consortium. The video is a combination of the yellow and blue fluorescence channels of a P_2N_2 consortium growing in the extended chamber microfluidic device.

References

1   Chen, Y., Kim, J. K., Hirning, A. J., Josić, K. & Bennett, M. R. Emergent genetic oscillations in synthetic microbial consortia. *Science* **349**, 986-989 (2015).

2   Block, D. H. S., Hussein, R., Liang, L. W. & Lim, H. N. Regulatory consequences of gene translocation in bacteria. *Nucleic Acids Research* **40**, 8979-8992 (2012).

3   Lamb, J. R., Patel, H., Montminy, T., Wagner, V. E. & Iglewski, B. H. Functional domains of the Rh1R transcriptional regulator of Pseudomonas aeruginosa. *Journal of Bacteriology* **185**, 7129-7139 (2003).

4   Burton, B. M., Williams, T. L. & Baker, T. A. ClpX-mediated remodeling of Mu transpososomes: Selective unfolding of subunits destabilizes the entire complex. *Molec Cell* **8**, 449-454 (2001).

5   Farrell, C. M., Baker, T. A. & Sauer, R. T. Altered specificity of a AAA plus protease. *Molec Cell* **25**, 161-166 (2007).

6   Flynn, J. M. *et al.* Overlapping recognition determinants within the ssrA degradation tag allow modulation of proteolysis. *Proc Natl Acad Sci USA* **98**, 10584-10589 (2001).

7   Wang, L. H., Weng, L. X., Dong, Y. H. & Zhang, L. H. Specificity and enzyme kinetics of the quorum-quenching N-acyl homoserine lactone lactonase (AHL-lactonase). *J Biol Chem* **279**, 13645-13651 (2004).

8   Thomas, P. W., Stone, E. M., Costello, A. L., Tierney, D. L. & Fast, W. The quorum-quenching lactonase from Bacillus thuringiensis is a metalloprotein. *Biochemistry* **44**, 7559-7569 (2005).

9   Volfson, D., Cookson, S., Hasty, J. & Tsimring, L. S. Biomechanical ordering of dense cell populations. *Proc Natl Acad Sci USA* **105**, 15346-15351 (2008).

10   Prindle, A. *et al.* Rapid and tunable post-translational coupling of genetic circuits. *Nature* **508**, 387-391 (2014).

11   Pai, A. & You, L. C. Optimal tuning of bacterial sensing potential. *Mol Syst Biol* **5**, 286 (2009).

12   Parsek, M. R., Val, D. L., Hanzelka, B. L., Cronan, J. E. & Greenberg, E. P. Acyl homoserine-lactone quorum-sensing signal generation. *Proc Natl Acad Sci USA* **96**, 4360-4365 (1999).

13   Schaefer, A. L., Val, D. L., Hanzelka, B. L., Cronan, J. E. & Greenberg, E. P. Generation of cell-to-cell signals in quorum sensing: Acyl homoserine lactone synthase activity of a purified Vibrio fescheri LuxI protein. *Proc Natl Acad Sci USA* **93**, 9505-9509 (1996).

14   Nagai, T. *et al.* A variant of yellow fluorescent protein with fast and efficient maturation for cell-biological applications. *Nat Biotechnol* **20**, 87-90 (2002).

15   Gedeon, T. & Bokes, P. Delayed Protein Synthesis Reduces the Correlation between mRNA and Protein Fluctuations. *Biophys J* **103**, 377-385 (2012).

16   Danino, T., Lo, J., Prindle, A., Hasty, J. & Bhatia, S. N. In Vivo Gene Expression Dynamics of Tumor-Targeted Bacteria. *Acs Synth Biol* **1**, 465-470 (2012).

17   Alnahhas, R. N. *et al.* Spatiotemporal dynamics of synthetic microbial consortia in microfluidic

devices. Accepted for publication in *ACS Synth Biol* (2019).